1 **Development and evaluation of a variably saturated flow model in the global**

2 **E3SM Land Model (ELM) Version 1.0**

3

4 **Gautam Bisht[1], William J. Riley[1], Glenn E. Hammond[2], and David M. Lorenzetti[3]**

5

6 [1]Climate & Ecosystem Sciences Division, Lawrence Berkeley National Laboratory,1

7 Cyclotron Road, Berkeley, California 94720, USA

8

9 [2]Applied Systems Analysis and Research Department, Sandia National Laboratories,

10 Albuquerque, NM 87185-0747, USA

11

12 [3]Sustainable Energy Systems Group, Lawrence Berkeley National Laboratory,1

13 Cyclotron Road, Berkeley, California 94720, USA

14

15 Correspondence to: Gautam Bisht (gbisht@lbl.gov)

16 **Abstract**

17 Improving global-scale model representations of coupled surface and groundwater

18 hydrology is important for accurately simulating terrestrial processes and predicting

19 climate change effects on water resources. Most existing land surface models,

20 including the default E3SM Land Model (ELMv0), which we modify here, routinely

21 employ different formulations for water transport in the vadose and pheratic zones.

22 In this work, we developed the Variably Saturated Flow Model (VSFM) in ELMv1 to

23 unify the treatment of soil hydrologic processes in the unsaturated and saturated

24 zones. VSFM was tested on three benchmark problems and results were evaluated

25 against observations and an existing benchmark model (PFLOTRAN). The ELMv1-

26 VSFM's subsurface drainage parameter, f_d , was calibrated to match an

27 observationally-constrained and spatially-explicit global water table depth (WTD)

28 product. An optimal f_d was obtained for 79% of global $1.9^0 \times 2.5^0$ gridcells, while the

29 remaining 21% of global gridcells had predicted WTD deeper than the

30 observationally-constrained estimate. Comparison with predictions using the default

31 f_d value demonstrated that calibration significantly improved prediction, primarily

32 by allowing much deeper WTDs. Model evaluation using the International Land Model

33 Benchmarking package (ILAMB) showed that improvements in WTD predictions did

34 not degrade model skill for any other metrics. We evaluated the computational

35 performance of the VSFM model and found that the model is about 30% more

36 expensive than the default ELMv0 with an optimal processor layout.

1   Introduction

37

38   Groundwater, which accounts for 30% of freshwater reserves globally, is a vital

39   human water resource. It is estimated that groundwater provides 20-30% of global

40   freshwater withdrawals (Petra, 2009; Zektser and Evertt, 2004), and that irrigation

41   accounts for ~70% of these withdrawals (Siebert et al., 2010). Climate change is

42   expected to impact the quality and quantity of groundwater in the future (Alley,

43   2001). As temporal variability of precipitation and surface water increases in the

44   future due to climate change, reliance on groundwater as a source of fresh water for

45   domestic, agriculture, and industrial use is expected to increase (Taylor et al., 2013).

46   Local environmental conditions modulate the impact of rainfall changes on

47   groundwater resources. For example, high intensity precipitation in humid areas may

48   lead to a decrease in groundwater recharge (due to higher surface runoff), while arid

49   regions are expected to see gains in groundwater storage (as infiltrating water

50   quickly travels deep into the ground before it can be lost to the atmosphere)

51   (Kundzewicz and Doli, 2009). Although global climate models predict changes in

52   precipitation over the next century (Marvel et al., 2017), few global models that

53   participated in the recent Coupled Model Inter-comparison Project (CMIP5; Taylor et

54   al. (2012)) were able to represent global groundwater dynamics accurately (e.g.

55   Swenson and Lawrence (2014))

56   Modeling studies have also investigated impacts, at watershed to global scale, on

57   future groundwater resources associated with land-use (LU) and land-cover (LC)

58   change (Dams et al., 2008) and ground water pumping (Ferguson and Maxwell, 2012;

59   Leng et al., 2015). Dams et al. (2008) predicted that LU changes would result in a small

60   mean decrease in subsurface recharge and large spatial and temporal variability in

61   groundwater depth for the Kleine Nete basin in Belgium. Ferguson and Maxwell

62   (2012) concluded that groundwater-fed irrigation impacts on water exchanges with

63   the atmosphere and groundwater resources can be comparable to those from a 2.5 °C

64   increase in air temperature for the Little Washita basin in Oklahoma, USA. By

65   performing global simulations of climate change scenarios using CLM4, Leng et al.

66   (2015) concluded that the water source (i.e., surface or groundwater) used for

67   irrigation depletes the corresponding water source while increasing the storage of
68   the other water source. Recently, Leng et al. (2017) showed that irrigation method
69   (drip, sprinkler, or flood) has impacts on water balances and water use efficiency in
70   global simulations.

71   Groundwater models are critical for developing understanding of
72   groundwater systems and predicting impacts of climate change (Green et al., 2011;
73   Kollet and Maxwell, 2008). Kollet and Maxwell (2008) identified critical zones, i.e.,
74   regions within the watershed with water table depths between $1 - 5$ m, where the
75   influence of groundwater dynamics was largest on surface energy budgets. Numerical
76   studies have demonstrated impacts of groundwater dynamics on several key Earth
77   system processes, including soil moisture (Chen and Hu, 2004; Liang et al., 2003;
78   Salvucci and Entekhabi, 1995; Yeh and Eltahir, 2005), runoff generation (Levine and
79   Salvucci, 1999; Maxwell and Miller, 2005; Salvucci and Entekhabi, 1995; Shen et al.,
80   2013), surface energy budgets (Alkhaier et al., 2012; Niu et al., 2017; Rihani et al.,
81   2010; Soylu et al., 2011), land-atmosphere interactions (Anyah et al., 2008; Jiang et
82   al., 2009; Leung et al., 2011; Yuan et al., 2008), vegetation dynamics (Banks et al.,
83   2011; Chen et al., 2010), and soil biogeochemistry (Lohse et al., 2009; Pacific et al.,
84   2011).

85   Recognizing the importance of groundwater systems on terrestrial processes,
86   groundwater models of varying complexity have been implemented in land surface
87   models (LSMs) in recent years. Groundwater models in current LSMs can be classified
88   into four categories based on their governing equations. Type-1 models assume a
89   quasi-steady state equilibrium of the soil moisture profile above the water table
90   (Hilberts et al., 2005; Koster et al., 2000; Walko et al., 2000). Type-2 models use a θ-
91   based (where θ is the water volume content) Richards equation in the unsaturated
92   zone coupled with a lumped unconfined aquifer model in the saturated zone.
93   Examples of one-dimensional Type-2 models include Liang et al. (2003), Yeh and
94   Eltahir (2005), Niu et al. (2007), and Zeng and Decker (2009). Examples of quasi
95   three-dimensional Type-2 models are York et al. (2002); Fan et al. (2007); Miguez-
96   Macho et al. (2007); and Shen et al. (2013). Type-3 models include a three-

97   dimensional representation of subsurface flow based on the variably saturated

98   Richards equation (Maxwell and Miller, 2005; Tian et al., 2012). Type-3 models

99   employ a unified treatment of hydrologic processes in the vadose and pheratic zones

100   but lump changes associated with water density and unconfined aquifer porosity into

101   a specific storage term. The fourth class (Type-4) of subsurface flow and reactive

102   transport models (e.g., PFLOTRAN (Hammond and Lichtner, 2010), TOUGH2 (Pruess

103   et al., 1999), and STOMP (White and STOMP, 2000)) combine a water equation of

104   state (EoS) and soil compressibility with the variably saturated Richards equation.

105   Type-4 models have not been routinely coupled with LSMs to address climate change

106   relevant research questions.

107   The Energy, Exascale, Earth System Model (E3SM) is a new Earth System

108   Modeling project sponsored by the U.S. Department of Energy (DOE). The E3SM

109   model started from the Community Earth System Model (CESM) version 1_3_beta10

110   (Oleson, 2013). Specifically, the initial version (v0) of the E3SM Land Model (ELM)

111   was based off the Community Land Model's (CLM's) tag 4_5_71. ELMv0 uses a Type-

112   2 subsurface hydrology model based on Zeng and Decker (2009). In this work, we

113   developed in ELMv1 a Type-4 Variably Saturated Flow model (VSFM) to provide a

114   unified treatment of soil hydrologic processes within the unsaturated and saturated

115   zones. The VSFM formulation is based on the isothermal single phase flow model of

116   PFLOTRAN (see Hammond and Lichtner (2010) for details regarding various modes

117   supported in PFLOTRAN). While PFLOTRAN is a massively parallel, three-

118   dimensional subsurface model, the VSFM is a serial, one-dimensional model that is

119   appropriate for climate scale applications.

120   This paper is organized into several sections: (1) brief review of the ELMv0

121   subsurface hydrology model; (2) overview of the VSFM formulation integrated in

122   ELMv1; (3) application of the new model formulation to three benchmark problems;

123   (4) development of a subsurface drainage parameterization necessary to predict

124   global water table depths (WTDs) comparable to recently released observationally-

125   constrained estimates; (5) comparison of ELMv1 global simulations with the default

126   subsurface hydrology model and VSFM against multiple observations using the

127   International Land Model Benchmarking package (ILAMB; Hoffman et al. (2017));

128   and (6) a summary of major findings.

129   **2   Methods**

130   **2.1   Current Model Formulation**

131   Water flow in the unsaturated zone is often described by the θ-based Richards

132   equation:

$$\frac{\partial \theta}{\partial t} = -\nabla \cdot \boldsymbol{q} - Q \tag{1}$$

133

134   where θ [m³ of water m⁻³ of soil] is the volumetric soil water content, t [s] is time, $\boldsymbol{q}$

135   [m s⁻¹] is the Darcy water flux, and Q [m³ of water m⁻³ of soil s⁻¹] is a soil moisture

136   sink term. The Darcy flux, $\vec{q}$, is given by

$$\boldsymbol{q} = -K\nabla(\psi + z) \tag{2}$$

137   where K [ms⁻¹] is the hydraulic conductivity, z [m] is height above some datum in the

138   soil column and ψ [m] is the soil matric potential. The hydraulic conductivity and soil

139   matric potential are modeled as non-linear function of volumetric soil moisture

140   following Clapp and Hornberger (1978):

$$K = \Theta_{ice} K_{sat} \left(\frac{\theta}{\theta_{sat}}\right)^{2B+3} \tag{3}$$

$$\psi = \psi_{sat} \left(\frac{\theta}{\theta_{sat}}\right)^{-B} \tag{4}$$

141

142   where K_{sat} [m s⁻¹] is saturated hydraulic conductivity, ψ_{sat} [m] is saturated soil

143   matric potential, B is a linear function of percentage clay and organic content (Oleson,

144   2013), and Θ_{ice} is the ice impedance factor (Swenson et al., 2012). ELMv0 uses the

145   modified form of Richards equation of Zeng and Decker (2009) that computes Darcy

146   flux as

$$\boldsymbol{q} = -K\nabla(\psi + z - C) \tag{5}$$

147   where C is a constant hydraulic potential above the water table, z_{∇}, given as

$$C = \psi_E + z = \psi_{sat}\left(\frac{\theta_E(z)}{\theta_{sat}}\right)^{-B} = \psi_{sat} + z_\nabla \qquad (6)$$

148   where ψ_E [m] is the equilibrium soil matric potential, θ_E [m³ m⁻³] is volumetric soil

149   water content at equilibrium soil matric potential, and z_∇ [m] is height of water table

150   above the reference datum. ELMv0 uses a cell-centered finite volume spatial

151   discretization and backward Euler implicit time integration. By default, ELMv0's

152   vertical discretization of a soil column yields 15 soil layers of exponentially varying

153   soil thicknesses that reach a depth of 42.1 m Only the first 10 soils layers (or top 3.8

154   m of each soil column), are hydrologically active, while thermal processes are

155   resolved for all 15 soils layers. The nonlinear Darcy flux is linearized using Taylor

156   series expansion and the resulting tridiagonal system of equations is solved by LU

157   factorization.

158   Flow in the saturated zone is modeled as an unconfined aquifer below the soil

159   column based on the work of Niu et al. (2007). Exchange of water between the soil

160   column and unconfined aquifer depends on the location of the water table. When the

161   water table is below the last hydrologically active soil layer in the column, a recharge

162   flux from the last soil layer replenishes the unconfined aquifer. A zero-flux boundary

163   condition is applied to the last hydrologically active soil layer when the water table is

164   within the soil column. The unconfined aquifer is drained by a flux computed based

165   on the SIMTOP scheme of Niu et al. (2007) with modifications to account for frozen

166   soils (Oleson, 2013).

167   **2.2 New VSFM Model Formulation**

168   In the VSFM formulation integrated in ELMv1, we use the mass conservative form of

169   the variably saturated subsurface flow equation (Farthing et al., 2003; Hammond and

170   Lichtner, 2010; Kees and Miller, 2002):

$$\frac{\partial(\phi s_w \rho)}{\partial t} = -\boldsymbol{\nabla} \cdot (\rho \boldsymbol{q}) - Q \qquad (7)$$

171   where ϕ [m³ m⁻³] is the soil porosity, s_w [-] is saturation, ρ [kg m⁻³] is water density,

172      $\boldsymbol{q}$ [m s⁻¹] is the Darcy velocity, and Q [kg m⁻³ s⁻¹] is a water sink. We restrict our model

Geoscientific
Model Development
Discussions

173   formulation to a one-dimensional system and the flow velocity is defined by Darcy's

174   law:

$$\boldsymbol{q} = -\frac{kk_r}{\mu}\boldsymbol{\nabla}(P + \rho gz) \tag{8}$$

175   where k [m²] is intrinsic permeability, k_r [-] is relative permeability, μ [Pa s] is

176   viscosity of water, P [Pa] is pressure], g [m s⁻²] is the acceleration due to gravity, and

177   z [m] is elevation above some datum in the soil column.

178   In order to close the system, a constitutive relationship is used to express soil

179   saturation and relative permeability as a function of soil matric pressure. Analytic

180   Water Retention Curves (WRCs) are used to model effective saturation (s_e)

$$s_e = \left(\frac{s_w - s_r}{1 - s_r}\right) \tag{9}$$

181   where s_w is soil saturation and s_r is residual soil saturation. We have implemented

182   Brooks and Corey (1964) (equation 10) and van Genuchten (1980) (equation 11)

183   WRCs:

$$s_e = \begin{cases} \left(\frac{-P_c}{P_c^0}\right)^{-\lambda} & if\ P_c < 0 \\ 1 & if\ P \geq 0 \end{cases} \tag{10}$$

$$s_e = \begin{cases} [1 + (\alpha|P_c|^n)]^{-m} & if\ P < 0 \\ 1 & if\ P \geq 0 \end{cases} \tag{11}$$

184   where P_c [Pa] is the capillary pressure and P_c^0 [Pa] is capillary pressure denoting air

185   entry point. The capillary pressure is computed as $P_c = P - P_{ref}$ where P_{ref} is P_c^0 for

186   Brooks and Corey WRC and typically the atmospheric pressure (=101,325 [Pa]) is

187   used for van Genuchten WRC. In addition, a smooth approximation of equation (10)

188   and (11) was developed to facilitate convergence of the nonlinear solver (Appendix

189   A). Relative soil permeability was modeled using the Mualem (1976) formulation:

$$\kappa_r(s_e) = \begin{cases} s_e^{0.5}\left[1 - \left(1 - s_e^{1/m}\right)^m\right] & if\ P < P_{ref} \\ 1 & if\ P \geq P_{ref} \end{cases} \tag{12}$$

190   Lastly, we used an EoS for water given by Tanaka et al. (2001):

$$\rho(P,T) = [1 + (k_0 + k_1T + k_2T^2)(P - P_{ref})]a_5\left[1 - \frac{(T + a_1)^2(T + a_2)}{a_3(T + a_4)}\right] \tag{13}$$

Geoscientific
Model Development
Discussions

191   where

$$k_0 = 50.74 \times 10^{-11} \text{ [Pa}^{-1}]$$

$$k_1 = -0.326 \times 10^{-11} \text{ [Pa}^{-1}\text{C}^{-1}]$$

$$k_2 = 0.00416 \times 10^{-11} \text{ [Pa}^{-1}\text{C}^2]$$

$$a_1 = -3.983035 \text{ [C]}$$

$$a_2 = 301.797 \text{ [C]}$$

$$a_3 = 522558.9 \text{ [C}^{-2}]$$

$$a_4 = 69.34881 \text{ [C]}$$

$$a_5 = 999.974950 \text{ [kg m}^{-3}]$$

192   Unlike the default subsurface hydrology model, the VSFM is applied over the
193   full sol depth (in the default model, 15 soils layers). The VSFM model replaces both
194   the θ-based Richards equation and the unconfined aquifer of the default model. In the
195   VSFM model, water table depth is diagnosed based on the vertical soil liquid pressure
196   profile. Like the default model, drainage flux is computed based on the modified
197   SIMTOP approach and is vertically distributed over the soil layers below the water
198   table.

199   **2.2.1   Discrete Equations**

200   We use a cell-centered finite volume discretization to decompose the spatial
201   domain, Ω, into N non-overlapping control volumes, Ω_n, such that $\Omega = \cup_{n=1}^{N} \Omega_i$ and Γ_n
202   represents the boundary of the n-th control volume. Applying a finite volume integral
203   to equation (7) and the divergence theorem yields

$$\frac{\partial}{\partial t} \int_{\Omega_n} (\phi s_w \rho) \, dV = - \int_{\Gamma_n} (\rho \boldsymbol{q}) \cdot d\boldsymbol{A} - \int_{\Omega_n} Q \tag{14}$$

204   The discretized form of the left hand side term and first term on the right hand side
205   of equation (14) are approximated as:
206

$$\frac{\partial}{\partial t} \int_{\Omega_n} (\phi s_w \rho) \, dV \approx \left(\frac{d}{dt} (\phi s_w \rho) \right) V_n \tag{15}$$

9

Geoscientific
Model Development
Discussions

$$\int_{\Gamma_n} (\rho \boldsymbol{q}) \cdot d\boldsymbol{A} \approx \sum_{n'} (\rho \boldsymbol{q})_{nn'} \cdot \boldsymbol{A}_{nn'} \tag{16}$$

207   After substituting equations (15) and (16) in equation (14), the resulting ordinary
208   differential equation for the variably saturated flow model is

$$\left(\frac{d}{dt}(\phi s_w \rho) \right) V_n = -\sum_{n'} (\rho \boldsymbol{q})_{nn'} \cdot \boldsymbol{A}_{nn'} - Q_n V_n \tag{17}$$

209   We perform temporal integration of equation (17) using the backward-Euler scheme:

$$\left(\frac{(\phi s_w \rho)_n^{t+1} - (\phi s_w \rho)_n^{t}}{\Delta t} \right) V_n = -\sum_{n'} (\rho \boldsymbol{q})_{nn'}^{t+1} \cdot \boldsymbol{A}_{nn'} - Q_n^{t+1} V_n \tag{18}$$

210   Rearranging terms of equation (18) results in a nonlinear equation for the unknown
211   pressure at timestep $t+1$ as

$$\left(\frac{(\phi s_w \rho)_n^{t+1} - (\phi s_w \rho)_n^{t}}{\Delta t} \right) V_n + \sum_{n'} (\rho \boldsymbol{q})_{nn'}^{t+1} \cdot \boldsymbol{A}_{nn'} + Q_n^{t+1} V_n = 0 \tag{19}$$

212   In this work, we find the solution to the system of nonlinear equations given by
213   equation (19) using Newton's method with the Portable, Extensible Toolkit for
214   Scientific Computing (PETSc) library (Balay et al., 2016). PETSc provides a suite of
215   data structures and routines for the scalable solution of partial differential equations.
216   A Smooth approximation of the Brooks and Corey (1964) (SBC) water retention curve
217   was developed to facilitate faster convergence of the nonlinear solver (Appendix A).

218   **2.3   VSFM single-column evaluation**

219   We tested the VSFM with three idealized 1-dimensional test problems. First, the
220   widely studied problem for 1D Richards equation of infiltration in dry soil by Celia et
221   al. (1990) was used. The problem setup consists of a 1.0 m long soil column with a
222   uniform initial pressure of −10.0 m (= 3535.5 Pa). Time invariant boundary
223   conditions applied at the top and bottom of soil column are −0.75 m (= 9399.1 Pa)
224   and −10.0 m (= 3535.5 Pa), respectively. The soil properties for this test are given in
225   Table 1. A vertical discretization of 0.01 m is used in this simulation.

226   Second, we simulated transient one-dimensional vertical infiltration in two-
227   layered soil system as described in Srivastava and Yeh (1991). The domain consisted

228   of a 2 m tall soil column divided equally in two soil types. Except soil permeability, all

229   other soil properties of the two soil types are the same. The bottom soil is 10 times

230   less permeable than the top (Table1). Unlike Srivastava and Yeh (1991), who used

231   exponential functions of soil liquid pressure to compute hydraulic conductivity and

232   soil saturation, we used Mualem (1976) and van Genuchten (1980) constitutive

233   relationships. Since our choice of constitutive relationships for this setup resulted in

234   absence of an analytical solution, we compared VSFM simulations against PFLOTRAN

235   results. The domain was discretized in 200 control volumes of equal soil thickness.

236   Two scenarios, wetting and drying, were modeled to test the robustness of the VSFM

237   solver robustness. Initial conditions for each scenario included a time invariant

238   boundary condition of 0 m (= 1.01325×10^5 Pa) for the lowest control volume and a

239   constant flux of 0.9 cm hr^{-1} and 0.1 cm hr^{-1} at the soil surface for wetting and drying

240   scenarios, respectively.

241   Third, we compare VSFM and PFLOTRAN predictions for soil under variably

242   saturated conditions. The 1-dimensional 1 m deep soil column was discretized in 100

243   equal thickness control volumes. A hydrostatic initial condition was applied such that

244   water table is 0.5 m below the soil surface. A time invariant flux of 2.5×10^{-5} m s^{-1} is

245   applied at the surface, while the lowest control volume has a boundary condition

246   corresponding to the initial pressure value at the lowest soil layer. The soil properties

247   used in this test are the same as those used in the first evaluation.

248   **2.4   Global Simulations and groundwater depth analysis**

249   We performed global simulations with ELMv1-VSFM at a spatial resolution of

250   1.9^0 (latitude) × 2.5^0 (longitude) with a 30 [min] time-step for 200 years, including a

251   180 year spinup and the last 20 years for analysis. The simulations were driven by

252   CRUNCEP meteorological forcing from 1991-2010 (Piao et al., 2012) and configured

253   to use prescribed satellite phenology.

254   For evaluation and calibration, we used the Fan et al. (2013) global ~1 km

255   horizontal resolution WTD dataset (hereafter F2013 dataset), which is based on a

256   combination of observations and hydrologic modeling. We aggregated the dataset to

257   the ELMv1-VSFM spatial resolution. ELM-VSFM's default vertical soil discretization

11

258   uses 15 soil layers to a depth of ~42 m, with an exponentially varying soil thickness.

259   However, ~13% of F2013 land gridcells have a water table deeper than 42 m. We

260   therefore modified ELMv1-VSFM to extend the soil column to a depth of 150 m with

261   59 soil layers; the first nine soil layer thicknesses were the same as described in

262   Oleson (2013) and the remaining layers (10-59) were set to a thickness of 3 m.

2.5   Estimation of the subsurface drainage parameterization

264   In the VSFM formulation, the dominant control on long-term GW depth is the

265   subsurface drainage flux, q_d [kg m^{-2} s^{-1}], which is calculated based on water table

266   depth, z_∇[m], (Niu et al. (2005)):

$$q_d = q_{d,max} exp(-f_d z_\nabla) \tag{20}$$

267   where $q_{d,max}$ [kg m^{-2} s^{-1}] is the maximum drainage flux that depends on gridcell slope

268   and f_d [m^{-1}] is an empirically-derived parameter. The subsurface drainage flux

269   formulation of Niu et al. (2005) is similar to the TOPMODEL formulation (Beven and

270   Kirkby, 1979) and assumes the water table is parallel to the soil surface. While

271   Sivapalan et al. (1987) derived $q_{d,max}$ as a function of lateral hydraulic anisotropy,

272   hydraulic conductivity, topographic index, and decay factor controlling vertical

273   saturated hydraulic conductivity, Niu et al. (2005) defined $q_{d,max}$ as a single

274   calibration parameter. ELMv0 uses $f_d = 2.5$ m^{-1} as a global constant and estimates

275   maximum drainage flux when WTD is at the surface as $q_{d,max} = 10 \sin(\beta)$ kg m^{-2} s^{-1}

276   . Of the two parameters, f_d and $q_{d,max}$, available for model calibration, we choose to

277   calibrate f_d because the uncertainty analysis by Hou et al. (2012) identified it as the

278   most significant hydrologic parameter in CLM4. To improve on the f_d parameter

279   values, we performed an ensemble of global simulations with f_d values of 0.1, 0.2, 0.5,

280   1.0, 2.5, 5.0, 10.0, and 20 m^{-1}. Each ensemble simulation was run for 200 years to

281   ensure an equilibrium solution, and the last 20 years were used for analysis. A non-

282   linear functional relationship between f_d and WTD was developed for each gridcell

283   and then the F2013 dataset was used to estimate an optimal f_d for each gridcell.

2.6 Global ELM-VSFM evaluation

284

285   With the optimal f_d values, we ran a ELM-VSFM simulation using the protocol

286 described above. We then used the International Land Model Benchmarking package

287 (ILAMB) to evaluate the ELMv1-VSFM predictions of surface energy budget, total

288 water storage anomalies (TWSA), and river discharge. ILAMB evaluates model

289 prediction bias, RMSE, and seasonal and diurnal phasing against multiple

290 observations of energy, water, and carbon cycles at in-situ, regional, and global scales.

291 Since ELM-VSFM simulations in this study did not include an active carbon cycle, we

292 used the following ILAMB benchmarks for water and energy cycles: (i) latent and

293 surface energy fluxes using site-level measurements from FLUXNET (Lasslop et al.,

294 2010) and globally from FLUXNET-MTE (Jung et al., 2009)); (ii) terrestrial water

295 storage anomaly (TWSA) from the Gravity Recovery And Climate Experiment

296 (GRACE) observations (Kim et al., 2009); and (iii) stream flow for the 50 largest global

297 river basins (Dai and Trenberth, 2002). We applied ILAMB benchmarks for ELMv1-

298 VSFM simulations with default and calibrated f_d to ensure improvements in WTD

299 predictions did not degrade model skill for other processes.

3   Results and discussion

300

3.1   VSFM single-column evaluation

301

302   For the 1D Richards equation infiltration in dry soil comparison, we evaluated

303 the solutions at 24-hr against those published by Celia et al. (1990) (Figure 1). The

304 VSFM solver accurately represented the sharp wetting front over time, where soil

305 hydraulic properties change dramatically due to non-linearity in the soil water

306 retention curve.

307   For the model evaluation of infiltration and drying in layered soil, the results of

308 the VSFM and PFLOTRAN are essentially identical. In both models and scenarios, the

309 higher permeability top soil responds rapidly to changes in the top boundary

310 condition and the wetting and drying fronts progressively travel through the less

Geoscientific
Model Development
Discussions

311   permeable soil layer until soil liquid pressure in the entire column reaches a new

312   steady state by about 100 h (Figure 2).

313   We also evaluated the VSFM predicted water table dynamics against PFLOTRAN

314   predictions from an initial condition of saturated soil below 0.5 m depth. The

315   simulated water table rises to 0.3 m depth by 1 day and reaches the surface by 2 days,

316   and the VSFM and PFLOTRAN predictions are essentially identical Figure 3. These

317   three evaluation simulations demonstrate the VSFM accurately represents soil

318   moisture dynamics under conditions relevant to ESM-scale prediction.

319   **3.2   Subsurface drainage parameterization estimation**

320   The simulated nonlinear WTD-f_d relationship is a result of the subsurface

321   drainage parameterization flux given by equation (20) (Figure 4(a) and (b)). For

322    $0.1 \leq f_d \leq 1$, the slope of the WTD-f_d relationship for all gridcells is log-log linear

323   with a slope of -1.0 ± 0.1. The log-log linear relationship breaks down for $f_d > 1$,

324   where the drainage flux becomes much smaller than infiltration and

325   evapotranspiration (Figure 4(c) and (d)). Thus, at larger f_d, the steady state z_∇

326   becomes independent of f_d and is determined by the balance of infiltration and

327   evapotranspiration.

328   For 79% of the global gridcells, the ensemble range of simulated WTD spanned

329   the F2013 dataset. The optimal value of f_d for each of these gridcells was obtained by

330   linear interpolation in the log-log space (e.g., Figure 4 (a)). For the remaining 21% of

331   gridcells where the shallowest simulated WTD across the range of f_d was deeper than

332   that in the F2013 dataset, the optimal f_d value was chosen as the one that resulted in

333   the lowest absolute WTD error (e.g., Figure 4 (b)). At large f_d values, the drainage flux

334   has negligible effect on WTD, yet simulated WTD is not sufficiently shallow to match

335   the F2013 observations, which indicates that either evapotranspiration is too large

336   or infiltration is too small. There was no difference in the mean percentage of sand

337   and clay content between grids cells with and without an optimal f_d value. The

338   optimal f_d has a global average of $1.60 \, \text{m}^{-1} \pm 2.68 \, \text{m}^{-1}$ and 72% of global gridcells have

339   an optimal f_d value lower than the global average (Figure 5).

3.3 Global simulation evaluation

The ELMv1-VSFM predictions are much closer to the F2013 dataset (Figure 6a) using optimal globally-distributed f_d values (Figure 6c) compared to the default f_d value (Figure 6b). The significant reduction in WTD bias (model – observation) is mostly due to improvement in the model's ability to accurately predict deep WTD using optimal f_d values. In the simulation using optimal globally-distributed f_d values, all gridcells with WTD bias > 3.7 m were those for which an optimal f_d was not found. The mean global bias, RMSE, and R^2 values were all improved in the new ELMv1-VSFM compared to the default model (Table 1). The 79% of global grid cells for which an optimal f_d value was estimated had significantly better water table prediction with a bias, RMSE, and R^2 of -0.04 m, 0.67m, and 0.99, respectively, as compared to the remaining 21% of global grid that had a bias, RMSE, and R^2 of -9.82 m, 18.08m, and 0.31, respectively. The simulated annual WTD range, which we define to be the difference between maximum and minimum WTD in a year, has a spatial mean and standard deviation of 0.32 m and 0.58 m, respectively, using optimal f_d values (Figure 7 (a)). The annual WTD range decreased by 0.24 m for the 79% of the grid cells for which an optimal f_d value was estimated (Figure 7 (b)).

Globally-averaged WTD in ELMv1-VSFM simulations with default f_d and optimal f_d values were 10.5 m and 20.1 m, respectively. Accurate prediction of deep WTD in the simulation with optimal f_d caused very small differences in near-surface soil moisture (Figure 8). The 79% of grid cells with an optimal f_d value had deeper globally-averaged WTDs than when using the default f_d value (24.3 m vs. 8.6 m). For these 79% of grid cells, the WTD was originally deep enough to not impact near-surface conditions (Kollet and Maxwell, 2008); therefore, further lowering of WTD led to negligible changes in near-surface hydrological conditions.

The International Land Model Benchmarking (ILAMB) package (Hoffman et al., 2017) provides a comprehensive evaluation of predictions of carbon cycle states and fluxes, hydrology, surface energy budgets, and functional relationships by comparison to a wide range of observations. We used ILAMB to evaluate the hydrologic and surface energy budget predictions from the new ELMv1-VSFM model

370   (Table 2). Optimal f_d values had inconsequential impacts on simulated surface

371   energy fluxes at site-level and global scales. Optimal f_d values led to improvement in

372   prediction of deep WTD (with a mean value of 24.3 m) for grid cells that had an

373   average WTD of 8.7 m in the simulation using default f_d values. Thus, negligible

374   differences in surface energy fluxes between the two simulations are consistent with

375   the findings of Kollet and Maxwell (2008), who identified decoupling of groundwater

376   dynamics and surface processes at a WTD of ∼10 m. There were slight changes in bias

377   and RMSE for predicted TWSA, but the ILAMB score remained unchanged. The TWSA

378   amplitude is lower for the simulation with optimal f_d values, consistent with the

379   associated decrease in annual WTD range. ELM's skill in simulating runoff for the 50

380   largest global watersheds remained unchanged.

381   Finally, we evaluated the computational costs of implementing VSFM in ELM,

382   and compared them to the default model. We performed 5-years long simulations for

383   default and VSFM using 96, 192, 384, 768, and 1536 cores on the Edison

384   supercomputer at the National Energy Research Scientific Computing Center. Using

385   an optimal processor layout, we found that ELMv1-VSFM is ∼30% more expensive

386   than the default ELMv1 model

3.4   Caveats and Future Work

388   The significant improvement in WTD prediction using optimal f_d values

389   demonstrates VSFM's capabilities to model hydrologic processes using a unified

390   physics formulation for unsaturated-saturated zones. However, several caveats

391   remain due to uncertainties in model structure, model parameterizations, and climate

392   forcing data.

393   In this study, we assumed a spatially homogeneous depth to bedrock (DTB) of

394   150 m. Recently, Brunke et al. (2016) incorporated a global ∼1 km dataset of soil

395   thickness and sedimentary deposits (Pelletier et al., 2016) in CLM4.5 to study the

396   impacts of soil thickness spatial heterogeneity on simulated hydrological and thermal

397   processes. While inclusion of heterogeneous DTB in CLM4.5 added more realism to

398   the simulation setup, no significant changes in simulated hydrologic and energy

399   fluxes were reported by Brunke et al. (2016). Presently, work is ongoing in the E3SM

400   project to include variable DTB within ELM and future simulations will examine the

401   impact of those changes on VSFM's prediction of WTD. Our use of the 'satellite

402   phenology' mode, which prescribes transient LAI profiles for each plant functional

403   type in the gridcell, ignored the likely influence of water cycle dynamics and nutrient

404   constraints on the C cycle (Ghimire et al., 2016; Zhu et al., 2016).

405   Lateral water redistribution impacts soil moisture dynamics (Bernhardt et al.,

406   2012), biogeochemical processes in the root zone (Grant et al., 2015), distribution of

407   vegetation structure (Hwang et al., 2012), and land-atmosphere interactions (Chen

408   and Kumar, 2001; Rihani et al., 2010). The ELMv1-VSMF developed in this study does

409   not include lateral water redistribution between soil columns and only simulates

410   vertical water transport. Lateral subsurface processes can be included in LSMs via a

411   range of numerical discretization approaches of varying complexity, e.g., adding

412   lateral water as source/sink terms in the 1D model, implementing an operator split

413   approach to solve vertical and lateral processes in a non-iterative approach (Ji et al.,

414   2017), or solving a fully coupled 3D model (Bisht et al., 2017; Bisht et al., 2018; Kollet

415   and Maxwell, 2008). Additionally, lateral transport of water can be implemented in

416   LSMs at a subgrid level (Milly et al., 2014) or grid cell level (Miguez-Macho et al.,

417   2007). The current implementation of VSFM is such that each processor solves the

418   variably saturated Richards equation for all independent soil columns as one single

419   problem. Thus, extension of VSFM to solve the tightly coupled 3D Richards equation

420   on each processor locally while accounting for lateral transport of water within grid

421   cells and among grid cells is straightforward. The current VSFM implementation can

422   also be easily extended to account for subsurface transport of water among grid cells

423   that are distributed across multiple processors by modeling lateral flow as a

424   source/sink in the 1D model. Tradeoffs between approaches to represent lateral

425   processes and computational costs need to be carefully studied before developing

426   quasi or fully three-dimensional land surface models.

4   Summary and Conclusion

Starting from the climate-scale land model ELMv0, we incorporated a unified physics formulation to represent soil moisture and groundwater dynamics that are solved using PETSc. Application of VSFM to three benchmarks problems demonstrated its robustness to simulated subsurface hydrologic processes in coupled unsaturated and saturated zones. Ensemble global simulations at $1.9^0 \times 2.5^0$ were performed for 200 years to obtain spatially heterogeneous estimate of a subsurface drainage parameter, f_d, that minimized the mismatch between predicted and observed WTD. In order to simulated the deepest water table reported in the Fan et al. (2013) dataset, we used 59 vertical soil layers that reached a depth of 150 m.

An optimal f_d was obtained for 79% of the grids cells in the domain. For the remaining 21% of grid cells, simulated WTD always remained deeper than observed. Calibration of f_d significantly improved global WTD prediction by reducing bias and RMSE and increasing R². Grids without an optimal f_d were the largest contributor of error in WTD predication. ILAMB benchmarks on simulations with default and optimal f_d showed negligible changes to surface energy fluxes, TWSA, and runoff. ILABM metrics ensured that model skill was not adversely impacted for all other processes when optimal f_d values were used to improve WTD prediction.

5   Appendix

5.1   Smooth approximation of Brooks-Corey water retention curve

The Brooks and Corey (1964) water retention curve of equation (10) has a discontinuous derivative at $P = P_c^0$. Figure A 1 shown an example. To improve convergence of the nonlinear solver at small capillary pressures, the smoothed Brooks-Corey function introduces a cubic polynomial, $B(P_c)$, in the neighborhood of P_c^0.

$$s_e = \begin{cases} (-\alpha P_c)^{-\lambda} & if\ P_c \le P_u \\ B(P_c) & if\ P_u < P_c < P_s \\ 1 & if\ P_s \le P_s \end{cases} \quad (21)$$

453   where the breakpoints P_u and P_s satisfy $P_u < P_c^0 < P_s \leq 0$. The smoothing

454   polynomial

$$B(P_c) = b_0 + b_1(P_c - P_s) + b_2(P_c - P_s)^2 + b_3(P_c - P_s)^3 \qquad (22)$$

455   introduces four more parameters, whose values follow from continuity. In particular

456   matching the saturated region requires $B(P_s) = b_0 = 1$, and a continuous derivative

457   at $P_c = P_s$ requires $B'(P_s) = b_1 = 0$. Similarly, matching the value and derivative at

458    $P_c = P_u$ requires

$$b_2 = \frac{-1}{\Delta^2}\left[3 - (\alpha P_u)^{-\lambda}\left(3 + \frac{\lambda\Delta}{P_u}\right)\right] \qquad (23)$$

$$b_3 = \frac{-1}{\Delta^3}\left[2 - (\alpha P_u)^{-\lambda}\left(2 + \frac{\lambda\Delta}{P_u}\right)\right] \qquad (24)$$

459   where $\Delta = P_u - P_s$. Note $P_u \leq \Delta < 0$.

460   In practice, setting P_u too close to P_c^0 can produce an unwanted local maximum

461   in the cubic smoothing regime, resulting in se > 1. Avoiding this condition requires

462   that $B(P_c)$ increase monotonically from $P_c = P_u$, where $B'(P_c) > 0$, to $P_c = P_s$, where

463    $B'(P_c) = 0$. Thus a satisfactory pair of breakpoints ensures

$$B'(P_c) = [P_c - P_s][2b_2 + 3b_3(P_c - P_s)] > 0 \qquad (25)$$

464   throughout $P_u \leq P_c < P_s$.

465   Let P_c^* denote a local extremum of B, so that $B'(P_c^*) = 0$. If $P_c^* \neq P_s$, it follows

466    $P_c^* - P_s = -2b_2/(3b_3)$. Rewriting equation 22, $B'(P_c) = (P_c - P_s)3b_3(P_c - P_c^*)$ shows

467   that $B'(P_c^*) > 0$ requires either: (1) $b_3 < 0$ and $P_c^* < P_u$; or (2) $b_3 > 0$ and $P_c^* > P_u$;.

468   The first possibility places P_c^* outside the cubic smoothing regime, and so does not

469   constrain the choice of P_u or P_s. The second possibility allows an unwanted local

470   extremum at $P_u < P_c^* < P_s$. In this case, $b_3 > 0$ implies $b_2 < 0$ (since $P_c^* < P_s \leq 0$).

471   Then since $B''(P_c^*) = -2b_2$, the local extremum is a maximum, resulting in $s_e(P_c^*) >$

472   1.

473   Given a breakpoint P_s, one strategy for choosing P_u is to guess a value, then

474   check whether the resulting b_2 and b_3 produces $P_u < P_c^* < P_s$. If so, P_u should be

475   made more negative. An alternative strategy is to choose P_u in order the guarantee

476   acceptable values for b_2 and b_3. One convenient choice forces $b_2 = 0$. Another picks

477   P_u in order to force $b_3 = 0$. Both of these reductions: (1) ensure $B(P_c)$ has a positive

Geoscientific
Model Development
Discussions

478   slope throughout the smoothing interval; (2) slightly reduce the computation cost of

479   finding $s_e(P_c)$ for P_c on the smoothing interval; and (3) significantly reduce the

480   computational cost of inverting the model, in order to find P_c as a function of s_e.

481   As shown in Figure A 1, the two reductions differ mainly in that setting $b_2 = 0$

482   seems to produce narrower smoothing regions (probably due to the fact that this

483   choice gives zero curvature at $P_c = P_s$, while $b_3 = 0$ yields a negative second

484   derivative there). However, we have not verified this observation analytically.

485   Both reductions require solving a nonlinear expression either equation (23) or

486   (24), for P_u. While details are beyond the scope of this paper, we note that we have

487   used a bracketed Newton-Raphson's method. The search switches to bisection when

488   Newton-Raphson would jump outside the bounds established by previous iterations,

489   and by the requirement $P_u < P_c^0$ In any event, since the result of this calculation may

490   be cached for use throughout the simulation, it need not be particularly efficient.

5.2   Residual equation of VSFM formulation

492   The residual equation for the VSFM formulation at $t + 1$ time level for n-th control

493   volume is given by

$$R_n^{t+1} \equiv \left(\frac{(\phi s_w \rho)_n^{t+1} - (\phi s_w \rho)_n^t}{\Delta t} \right) V_n + \sum_{n'} (\rho \boldsymbol{q})_{nn'}^{t+1} \cdot \boldsymbol{A}_{nn'} + Q_n^{t+1} V_n = 0 \qquad (26)$$

494   where ϕ [mm³ mm³] is the soil porosity, s_w [-] is saturation, ρ [kg m⁻³] is water

495   density, $\vec{q}_{nn'}$ [m s⁻¹] is the Darcy flow velocity between n-th and n'-th control

496   volumes, $A_{nn'}$ [m s⁻¹] is the interface face area between n-th and n'-th control

497   volumes Q [kg m⁻³ s⁻¹] is a sink of water. The Darcy velocity is computed as

$$\boldsymbol{q}_{nn'} = - \left(\frac{k k_r}{\mu} \right)_{nn'} \left[\frac{P_{n'} - P_n - \rho_{nn'}(\boldsymbol{g} \cdot \boldsymbol{d}_{nn'})}{d_n + d_{n'}} \right] \boldsymbol{n}_{nn'} \qquad (27)$$

498   where κ [m⁻²] is intrinsic permeability, κ_r [-] is relative permeability, μ [Pa s] is

499   viscosity of water, P [Pa] is pressure], $\boldsymbol{g}$ [m s⁻²] is the acceleration due to gravity,

500   d_n[m] and $d_{n'}$ [m] is distance between centroid of n-th and n'-th control volume to

501   the common interface between the two control volumes, $\boldsymbol{d}_{nn'}$ is a distance vector

502   joining centroid of n-th and n'-th control volume, and $\boldsymbol{n}_{nn'}$ is a unit normal vector

503   joining centroid of n-th and n'-th control volume.

504   The density at the interface of control volume, $\rho_{nn'}$, is computed as inverse

505   distance weighted average by

$$\rho_{nn'} = \omega_{n'}\rho_n + \omega_n\rho_{n'} \tag{28}$$

506   where ω_n and $\omega_{n'}$ are given by

$$\omega_n = \frac{d_n}{d_n + d_{n'}} = (1 - \omega_{n'}) \tag{29}$$

507   The first term on the RHS of equation 27 is computed as the product of distance

508   weighted harmonic average of intrinsic permeability, $k_{nn'}$, and upwinding of

509     $k_r/\mu \ (= \lambda)$ as

$$\left(\frac{kk_r}{\mu}\right)_{nn'} = k_{nn'}\left(\frac{k_r}{\mu}\right)_{nn'} = \left[\frac{k_n k_{n'}(d_n + d_{n'})}{k_n d_{n'} + k_{n'} d_n}\right]\lambda_{nn'} \tag{30}$$

510   where

$$\lambda_{nn'} = \begin{cases} (k_r/\mu)_n & if \ \vec{q}_{nn'} > 0 \\ (k_r/\mu)_{n'} & otherwise \end{cases} \tag{31}$$

511   By substituting equation 28, 29 and 30 in equation 27, we obtain

$$\boldsymbol{q}_{nn'} = -\left[\frac{k_n k_{n'}}{k_n d_{n'} + k_{n'} d_n}\right]\lambda_{nn'}[P_{n'} - P_n - \rho_{nn'}(\boldsymbol{g}.\boldsymbol{d}_{nn'})]\boldsymbol{n}_{nn'} \tag{32}$$

512

5.3 Jacobian equation of VSFM formulation

514   The discretized equations of VSFM leads to a system of nonlinear equations given by

515     $\boldsymbol{R}^{t+1}(\boldsymbol{P}^{t+1}) = \boldsymbol{0}$, which are solved using Newton's method using the Portable,

516   Extensible Toolkit for Scientific Computing (PETSc) library. The algorithm of

517   Newton's method requires solution of the following linear problem

$$\boldsymbol{J}^{t+1,k}(\boldsymbol{P}^{t+1,k})\,\Delta\boldsymbol{P}^{t+1,k} = -\boldsymbol{R}^{t+1,k}(\boldsymbol{P}^{t+1,k}) \tag{33}$$

518   where $\boldsymbol{J}^{t+1,k}(\boldsymbol{P}^{t+1,k})$ is the Jacobian matrix. In VSFM, the Jacobian matrix is

519   computed analytically. The contribution to the diagonal and off-diagonal entry of the

520   Jacobian matrix from n-th residual equations are given by

$$J_{nn} = \frac{\partial R_n}{\partial P_n} = \left(\frac{V_n}{\Delta t}\right)\frac{\partial(\rho\phi s_w)}{\partial P_n} + \sum_{n'}\frac{\partial(\rho\boldsymbol{q})_{nn'}}{\partial P_n}A_{nn'} + \frac{\partial Q_n^{t+1}}{\partial P_n}V_n \tag{34}$$

Geoscientific
Model Development
Discussions

$$J_{nn'} = \frac{\partial R_n}{\partial P_{n'}} = \sum_{n'} \frac{\partial (\rho \boldsymbol{q})_{nn'}}{\partial P_{n'}} \boldsymbol{A}_{nn'} + \frac{\partial Q_n^{t+1}}{\partial P_{n'}} V_n \tag{35}$$

521   The derivative of the accumulation term in J_{nn} is computed as

$$\frac{\partial (\rho \phi s_w)}{\partial P_n} = \phi s_w \frac{\partial \rho}{\partial P_n} + \rho s_w \frac{\partial \phi}{\partial P_n} + \rho \phi \frac{\partial s_w}{\partial P_n} \tag{36}$$

522   The derivative of flux between n-th and n'-th control volume with respect to

523   pressure of each control volume is given as

$$\frac{\partial (\rho \boldsymbol{q})_{nn'}}{\partial P_n} = \rho_{nn'} \frac{\partial \boldsymbol{q}_{nn'}}{\partial P_n} + \boldsymbol{q}_{nn'} \omega_n \frac{\partial \rho_n}{\partial P_n} \tag{37}$$

524

$$\frac{\partial (\rho \boldsymbol{q})_{nn'}}{\partial P_{n'}} = \rho_{nn'} \frac{\partial \boldsymbol{q}_{nn'}}{\partial P_{n'}} + \boldsymbol{q}_{nn'} \omega_{n'} \frac{\partial \rho_{n'}}{\partial P_{n'}} \tag{38}$$

525   Lastly, the derivative of Darcy velocity between n-th and n'-th control volume with

526   respect to pressure of each control volume is given as

$$\frac{\partial \boldsymbol{q}_{nn'}}{\partial P_n} = \left[\frac{k_n k_{n'}}{k_n d_{n'} + k_{n'} d_n)} \right] \lambda_{nn'} \left[1 + \omega_n (\boldsymbol{g} . \boldsymbol{d}_{nn'}) \frac{\partial \rho_n}{\partial P_n} \right] \boldsymbol{n}_{nn'} + \boldsymbol{q}_{nn'} \frac{\partial \big(ln(\lambda_{nn'}) \big)}{\partial P_n} \tag{39}$$

$$\frac{\partial \boldsymbol{q}_{nn'}}{\partial P_{n'}} = \left[\frac{k_n k_{n'}}{k_n d_{n'} + k_{n'} d_n)} \right] \lambda_{nn'} \left[-1 + \omega_n (\boldsymbol{g} . \boldsymbol{d}_{nn'}) \frac{\partial \rho_{n'}}{\partial P_{n'}} \right] \boldsymbol{n}_{nn'} \\ + \boldsymbol{q}_{nn'} \frac{\partial \big(ln(\lambda_{nn'}) \big)}{\partial P_{n'}} \tag{40}$$

527

6   Code availability

529   The standalone VSFM code is available at https://github.com/MPP-LSM/MPP. The

530   ELM-VSFM code will be made available with the public release of E3SM model in

531   April, 2018.

7   Competing interests

533   The authors declare that they have no conflict of interest.

534

8 Acknowledgements

540

9   Tables

Table 1 Bias, root mean square error (RMSE), and correlation (R^2) between simulated water table depth and Fan et al. (2013) data.

	Bias [m]	RMSE [m]	R^2
For all grids in ELM simulation with default f_{drain}	-10.3	21.3	0.28
For all grids in ELM simulation with optimal f_{drain}	2.10	8.33	0.91
For 79% grids with optimal f_{drain} in ELM simulation with optimal f_{drain}	-0.04	0.67	0.99
For 21% grids without optimal f_{drain} in ELM simulation with optimal f_{drain}	-9.82	18.08	0.31

546 **Table 2 ILAMB benchmark scores for latent heat flux (LH), sensible heat flux**

547 **(SH), total water storage anomaly (TWSA), and surface runoff. The calculation**

548 **of ILAMB metrics and scores are described at http://redwood.ess.uci.edu/.**

	Data Source	Simulation with default f_d			Simulation with optimal f_d		
		Bias	RMSE	ILAMB Score	Bias	RMSE	ILAMB Score
LH	FLUXNET	10.1 [Wm^{-2}]	21.0 [Wm^{-2}]	0.68	9.5 [Wm^{-2}]	21.3 [Wm^{-2}]	0.68
	GBAF	7.1 [Wm^{-2}]	16.3 [Wm^{-2}]	0.81	6.3 [Wm^{-2}]	16.3 [Wm^{-2}]	0.81
SH	FLUXNET	6.7 [Wm^{-2}]	22.5 [Wm^{-2}]	0.66	7.1 [Wm^{-2}]	22.8 [Wm^{-2}]	0.65
	GBAF	6.9 [Wm^{-2}]	21.2 [Wm^{-2}]	0.71	7.6 [Wm^{-2}]	21.7 [Wm^{-2}]	0.70
TWSA	GRACE	1.3 [cm]	7.8 [cm]	0.48	3.0 [cm]	9.6 [cm]	0.48
Runoff	Dai	-0.26 [kg $^{m-2}$ d^{-1}]	0.91 [m^{-2}m^{-2} d^{-1}]	0.52	-0.23 [kg m^{-2} d^{-1}]	0.88 [kg m^{-2} d^{-1}]	0.50

549

550

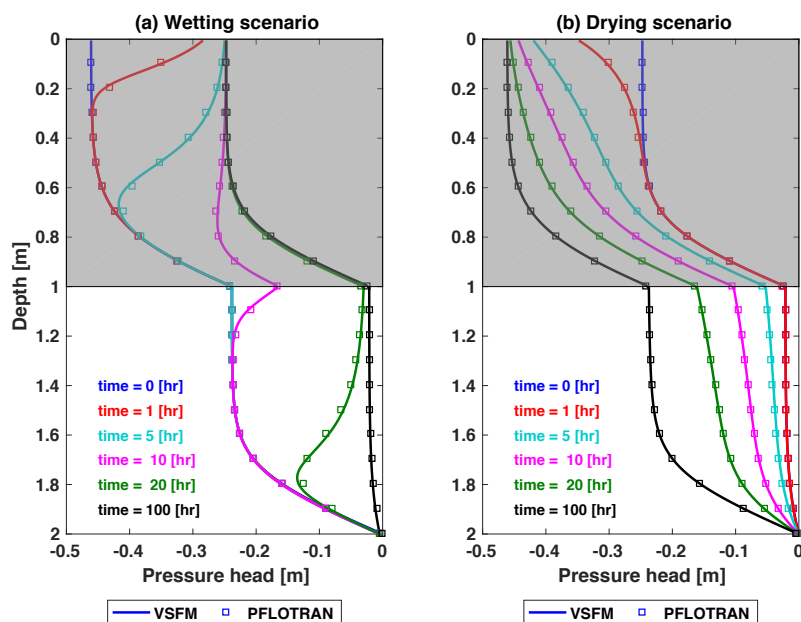## 10 Figures
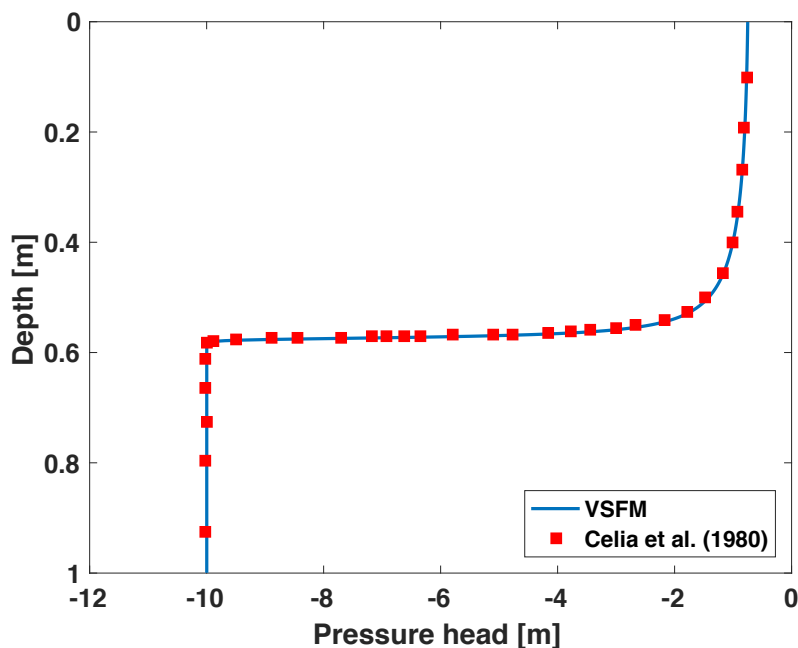
Figure 1. Comparison of VSFM simulated pressure profile (blue line) against data (red square) reported in Celia et al. (1990) at time = 24 hr for infiltration in a dry soil column. Initial pressure condition is shown by green line.
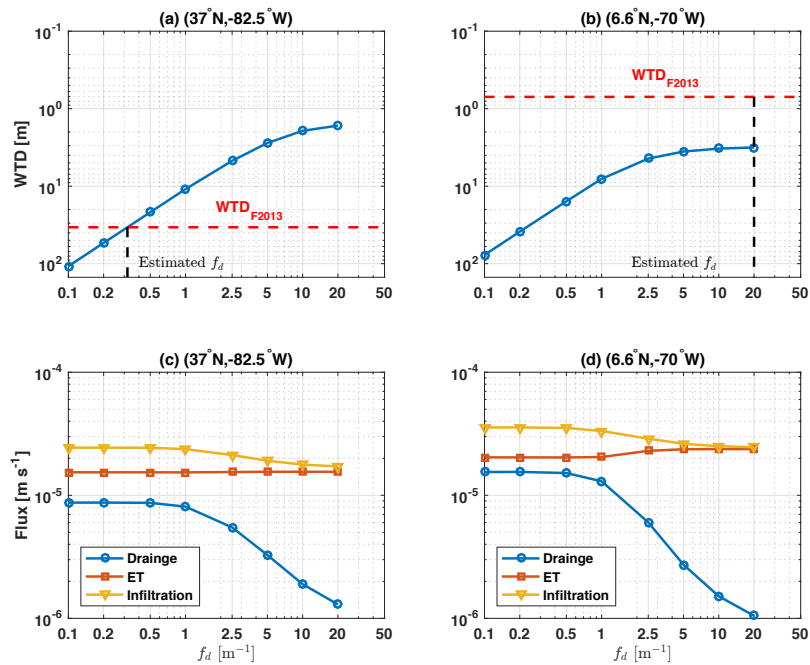
556

Figure 2. Transient liquid pressure simulated for a two layer soil system by VSFM (solid line) and PFLOTRAN (square) for wetting (left) and drying (right) scenarios.
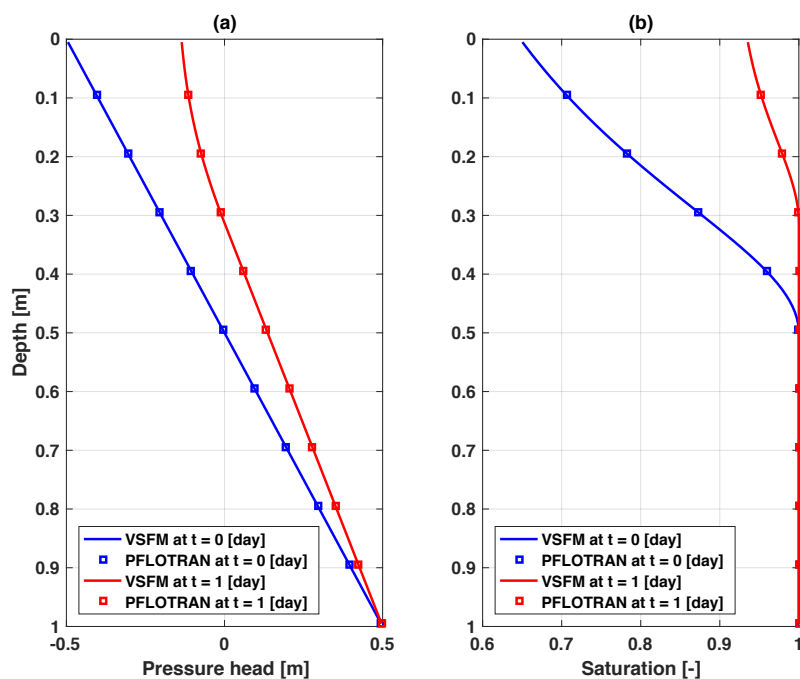
Figure 3. Transient liquid pressure (a) and soil saturation (b) simulated by VSFM (solid line) and PFLOTRAN (square) for the water table dynamics test problem.

Figure 4. (a-b) The nonlinear relationship between simulated water table depth (WTD) and f_d for two gridcells within ELM's global grid. WTD from the Fan et al. (2013) dataset and optimal f_d for the two gridcells are shown with a dashed red and dashed black lines, respectively. (c-d) The simulated drainage, evapotranspiration, and infiltration fluxes as functions of optimal f_d for the two ELM gridcells.
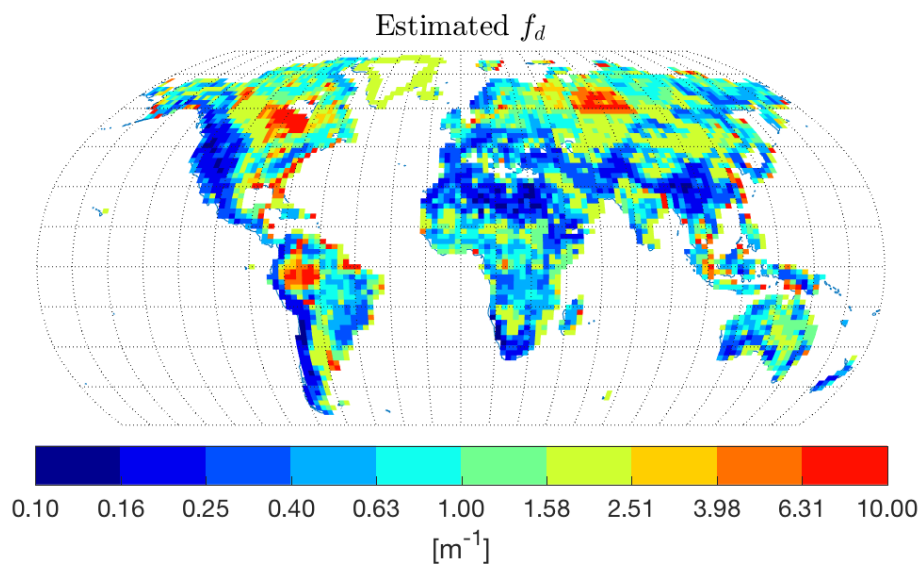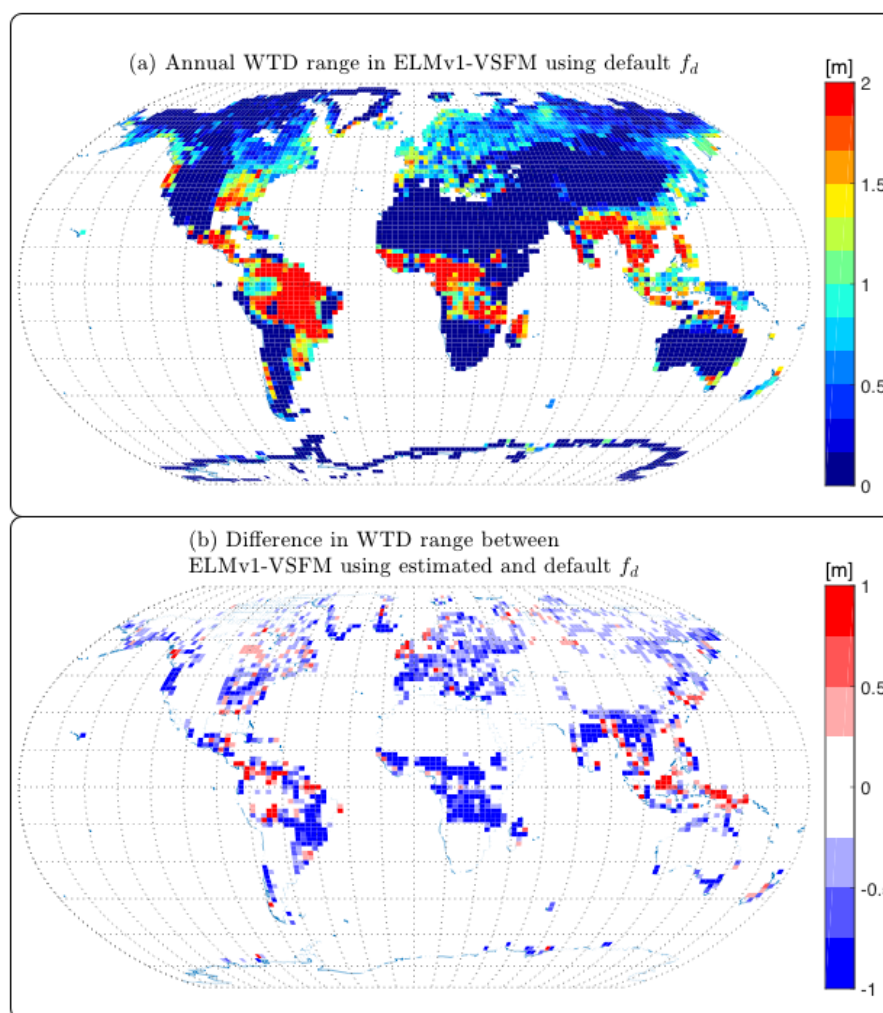
Figure 5. Global estimate of f_d.

574
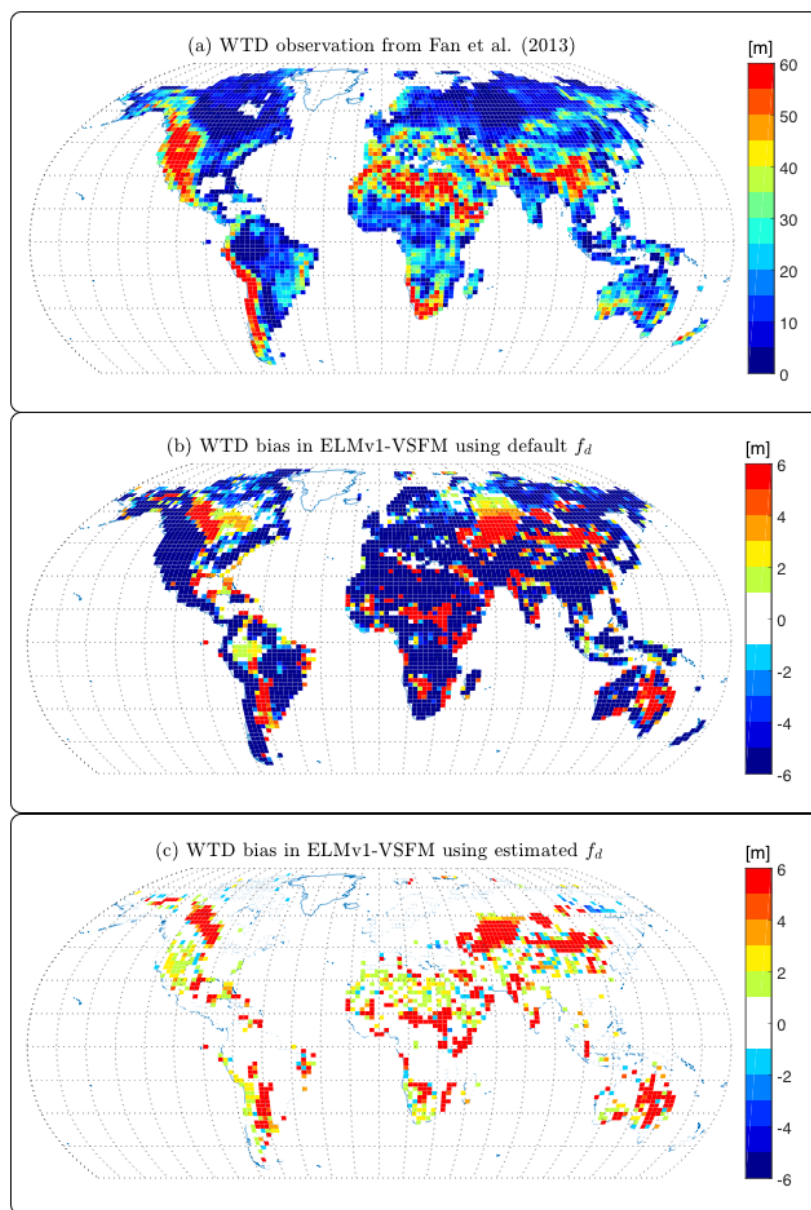
Figure 6. (a) Water table depth observation from Fan et al. (2013); (b) Water table depth biases (=Model – Obs) from ELMv1-VSFM using default spatially homogeneous f_d; and (c) Water table depth biases from ELMv1-VSFM using spatially heterogeneous f_d.
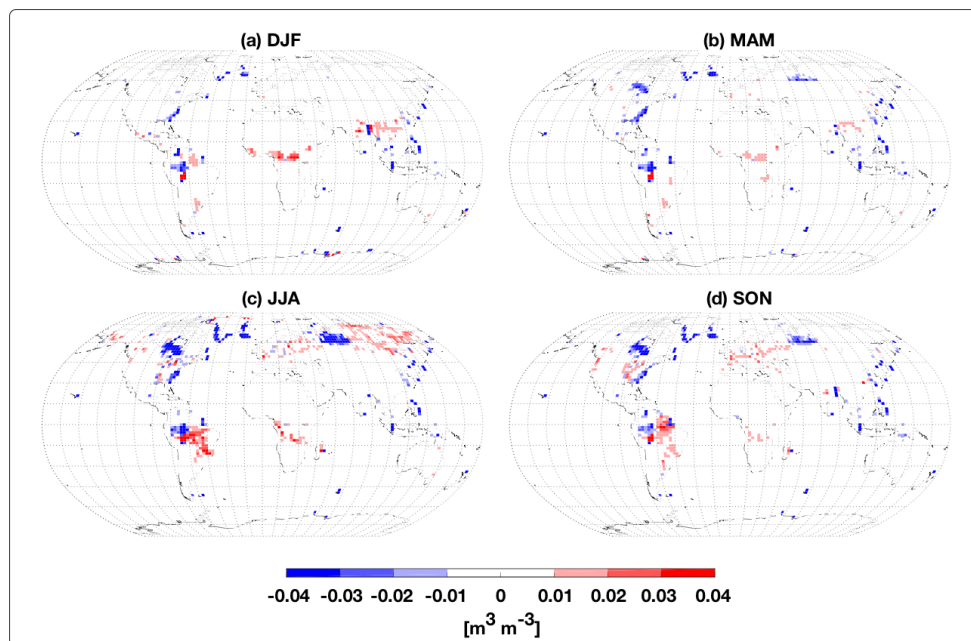
579

580

Figure 7. (a) Annual range of water table depth for ELMv1-VSFM simulation

with spatially heterogeneous estimates of f_d and (b) Difference in annual

water table depth range between simulations with optimal and default f_d.

584

585

Figure 8. Seasonal monthly mean soil moisture differences for top 10 cm between ELMv1-VSFM simulations with optimal and default f_d values.

588

589
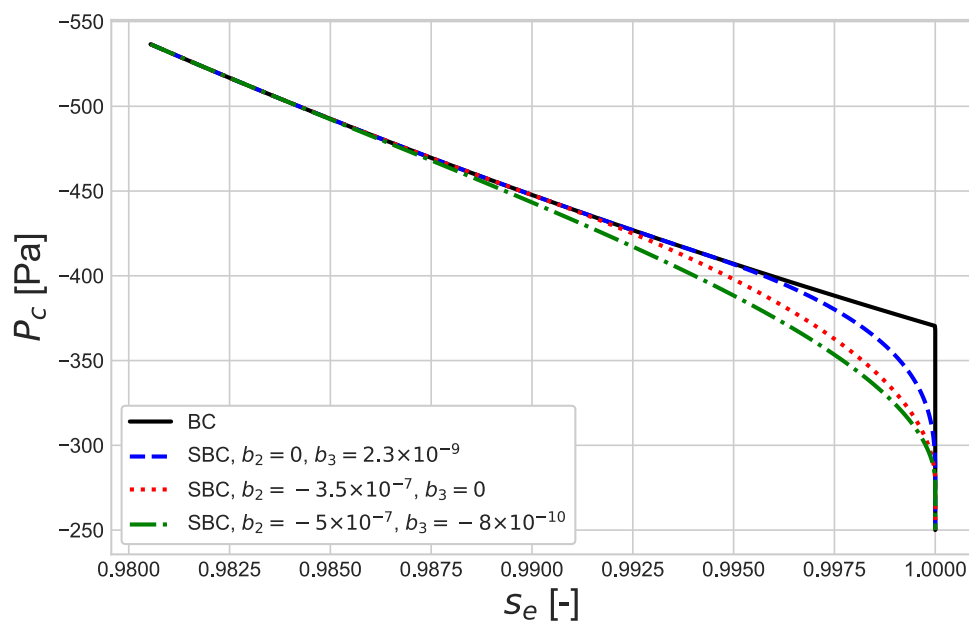
590

591 **Figure A 1 The Brooks-Corey water rendition curve for estimating liquid saturation, s_e,**

592 **as a function of capillary pressure, P_c, shown in solid black line and smooth**

593 **approximation of Brooks-Corey (SBC) are shown in dashed line.**

594

Geoscientific
Model Development
Discussions

595 **References**

596 Alkhaier, F., Flerchinger, G. N., and Su, Z.: Shallow groundwater effect on land surface
597 temperature and surface energy balance under bare soil conditions: modeling and
598 description, Hydrol. Earth Syst. Sci., 16, 1817-1831, 2012.
599 Alley, W. M.: Ground Water and Climate, Ground Water, 39, 161-161, 2001.
600 Anyah, R. O., Weaver, C. P., Miguez-Macho, G., Fan, Y., and Robock, A.: Incorporating
601 water table dynamics in climate modeling: 3. Simulated groundwater influence on
602 coupled land-atmosphere variability, Journal of Geophysical Research: Atmospheres,
603 113, n/a-n/a, 2008.
604 Balay, S., Abhyankar , S., Adams, M. F., Brown, J., Brune, P., Buschelman, K., Dalcin, L.,
605 Eijkhout, V., Gropp, W. D., Kaushik, D., Knepley, M. G., McInnes, L. C., Rupp, K., Smith,
606 B. F., Zampini, S., Zhang, H., and Zhang, H.: PETSc Users Manual, Argonne National
607 LaboratoryANL-95/11 - Revision 3.7, 1-241 pp., 2016.
608 Banks, E. W., Brunner, P., and Simmons, C. T.: Vegetation controls on variably
609 saturated processes between surface water and groundwater and their impact on the
610 state of connection, Water Resources Research, 47, n/a-n/a, 2011.
611 Bernhardt, M., Schulz, K., Liston, G. E., and Zängl, G.: The influence of lateral snow
612 redistribution processes on snow melt and sublimation in alpine regions, Journal of
613 Hydrology, 424–425, 196-206, 2012.
614 Beven, K. J. and Kirkby, M. J.: A physically based, variable contributing area model of
615 basin hydrology / Un modèle à base physique de zone d'appel variable de l'hydrologie
616 du bassin versant, Hydrological Sciences Bulletin, 24, 43-69, 1979.
617 Bisht, G., Huang, M., Zhou, T., Chen, X., Dai, H., Hammond, G. E., Riley, W. J., Downs, J. L.,
618 Liu, Y., and Zachara, J. M.: Coupling a three-dimensional subsurface flow and transport
619 model with a land surface model to simulate stream–aquifer–land interactions
620 (CP v1.0), Geosci. Model Dev., 10, 4539-4562, 2017.
621 Bisht, G., Riley, W. J., Wainwright, H. M., Dafflon, B., Yuan, F., and Romanovsky, V. E.:
622 Impacts of microtopographic snow redistribution and lateral subsurface processes
623 on hydrologic and thermal states in an Arctic polygonal ground ecosystem: a case
624 study using ELM-3D v1.0, Geosci. Model Dev., 11, 61-76, 2018.
625 Brooks, R. H. and Corey, A. T.: Hydraulic properties of porous media, Colorado State
626 University, Fort Collins, CO, 1964.
627 Brunke, M. A., Broxton, P., Pelletier, J., Gochis, D., Hazenberg, P., Lawrence, D. M.,
628 Leung, L. R., Niu, G.-Y., Troch, P. A., and Zeng, X.: Implementing and Evaluating Variable
629 Soil Thickness in the Community Land Model, Version 4.5 (CLM4.5), Journal of
630 Climate, 29, 3441-3461, 2016.
631 Celia, M. A., Bouloutas, E. T., and Zarba, R. L.: A general mass-conservative numerical
632 solution for the unsaturated flow equation, Water Resources Research, 26, 1483-
633 1496, 1990.
634 Chen, J. and Kumar, P.: Topographic Influence on the Seasonal and Interannual
635 Variation of Water and Energy Balance of Basins in North America, Journal of Climate,
636 14, 1989-2014, 2001.
637 Chen, X. and Hu, Q.: Groundwater influences on soil moisture and surface evaporation,
638 Journal of Hydrology, 297, 285-300, 2004.

Geoscientific
Model Development
Discussions

Open Access

639   Chen, Y., Chen, Y., Xu, C., Ye, Z., Li, Z., Zhu, C., and Ma, X.: Effects of ecological water
640   conveyance on groundwater dynamics and riparian vegetation in the lower reaches
641   of Tarim River, China, Hydrological Processes, 24, 170-177, 2010.
642   Clapp, R. B. and Hornberger, G. M.: Empirical equations for some soil hydraulic
643   properties, Water Resources Research, 14, 601-604, 1978.
644   Dai, A. and Trenberth, K. E.: Estimates of Freshwater Discharge from Continents:
645   Latitudinal and Seasonal Variations, Journal of Hydrometeorology, 3, 660-687, 2002.
646   Dams, J., Woldeamlak, S. T., and Batelaan, O.: Predicting land-use change and its
647   impact on the groundwater system of the Kleine Nete catchment, Belgium, Hydrol.
648   Earth Syst. Sci., 12, 1369-1385, 2008.
649   Fan, Y., Li, H., and Miguez-Macho, G.: Global Patterns of Groundwater Table Depth,
650   Science, 339, 940-943, 2013.
651   Fan, Y., Miguez-Macho, G., Weaver, C. P., Walko, R., and Robock, A.: Incorporating
652   water table dynamics in climate modeling: 1. Water table observations and
653   equilibrium water table simulations, Journal of Geophysical Research: Atmospheres,
654   112, n/a-n/a, 2007.
655   Farthing, M. W., Kees, C. E., and Miller, C. T.: Mixed finite element methods and higher
656   order temporal approximations for variably saturated groundwater flow, Advances
657   in Water Resources, 26, 373-394, 2003.
658   Ferguson, I. M. and Maxwell, R. M.: Human impacts on terrestrial hydrology: climate
659   change versus pumping and irrigation, Environmental Research Letters, 7, 044022,
660   2012.
661   Ghimire, B., Riley, W. J., Koven, C. D., Mu, M., and Randerson, J. T.: Representing leaf
662   and root physiological traits in CLM improves global carbon and nitrogen cycling
663   predictions, Journal of Advances in Modeling Earth Systems, 8, 598-613, 2016.
664   Grant, R. F., Humphreys, E. R., and Lafleur, P. M.: Ecosystem CO_2 and CH_4 exchange in
665   a mixed tundra and a fen within a hydrologically diverse Arctic landscape: 1. Modeling
666   versus measurements, Journal of Geophysical Research: Biogeosciences, 120, 1366-
667   1387, 2015.
668   Green, T. R., Taniguchi, M., Kooi, H., Gurdak, J. J., Allen, D. M., Hiscock, K. M., Treidel, H.,
669   and Aureli, A.: Beneath the surface of global change: Impacts of climate change on
670   groundwater, Journal of Hydrology, 405, 532-560, 2011.
671   Hammond, G. E. and Lichtner, P. C.: Field-scale model for the natural attenuation of
672   uranium at the Hanford 300 Area using high-performance computing, Water
673   Resources Research, 46, n/a-n/a, 2010.
674   Hilberts, A. G. J., Troch, P. A., and Paniconi, C.: Storage-dependent drainable porosity
675   for complex hillslopes, Water Resources Research, 41, n/a-n/a, 2005.
676   Hoffman, F. M., Koven, C. D., Keppel-Aleks, G., Lawrence, D. M., Riley, W. J., Randerson,
677   J. T., Ahlstrom, A., Abramowitz, G., Baldocchi, D. D., Best, M. J., Bond-Lamberty, B.,
678   Kauwe}, M. G. D., Denning, A. S., Desai, A. R., Eyring, V., Fisher, J. B., Fisher, R. A.,
679   Gleckler, P. J., Huang, M., Hugelius, G., Jain, A. K., Kiang, N. Y., Kim, H., Koster, R. D.,
680   Kumar, S. V., Li, H., Luo, Y., Mao, J., McDowell, N. G., Mishra, U., Moorcroft, P. R., Pau, G.
681   S. H., Ricciuto, D. M., Schaefer, K., Schwalm, C. R., Serbin, S. P., Shevliakova, E., Slater,
682   A. G., Tang, J., Williams, M., Xia, J., Xu, C., Joseph, R., and Koch, D.: International Land
683   Model Benchmarking (ILAMB) 2016 Workshop Report, U.S. Department of Energy,
684   Office of Science, 159 pp., 2017.

Geoscientific
Model Development
Discussions

685   Hou, Z., Huang, M., Leung, L. R., Lin, G., and Ricciuto, D. M.: Sensitivity of surface flux
686   simulations to hydrologic parameters based on an uncertainty quantification
687   framework applied to the Community Land Model, Journal of Geophysical Research:
688   Atmospheres, 117, n/a-n/a, 2012.
689   Hwang, T., Band, L. E., Vose, J. M., and Tague, C.: Ecosystem processes at the watershed
690   scale: Hydrologic vegetation gradient as an indicator for lateral hydrologic
691   connectivity of headwater catchments, Water Resources Research, 48, n/a-n/a, 2012.
692   Ji, P., Yuan, X., and Liang, X.-Z.: Do Lateral Flows Matter for the Hyperresolution Land
693   Surface Modeling?, Journal of Geophysical Research: Atmospheres, doi:
694   10.1002/2017JD027366, 2017. n/a-n/a, 2017.
695   Jiang, X., Niu, G.-Y., and Yang, Z.-L.: Impacts of vegetation and groundwater dynamics
696   on warm season precipitation over the Central United States, Journal of Geophysical
697   Research: Atmospheres, 114, n/a-n/a, 2009.
698   Jung, M., Reichstein, M., and Bondeau, A.: Towards global empirical upscaling of
699   FLUXNET eddy covariance observations: validation of a model tree ensemble
700   approach using a biosphere model, Biogeosciences, 6, 2001-2013, 2009.
701   Kees, C. E. and Miller, C. T.: Higher order time integration methods for two-phase flow,
702   Advances in Water Resources, 25, 159-177, 2002.
703   Kim, H., Yeh, P. J. F., Oki, T., and Kanae, S.: Role of rivers in the seasonal variations of
704   terrestrial water storage over global basins, Geophysical Research Letters, 36, n/a-
705   n/a, 2009.
706   Kollet, S. J. and Maxwell, R. M.: Capturing the influence of groundwater dynamics on
707   land surface processes using an integrated, distributed watershed model, Water
708   Resources Research, 44, n/a-n/a, 2008.
709   Koster, R. D., Suarez, M. J., Ducharne, A., Stieglitz, M., and Kumar, P.: A catchment-
710   based approach to modeling land surface processes in a general circulation model: 1.
711   Model structure, Journal of Geophysical Research: Atmospheres, 105, 24809-24822,
712   2000.
713   Kundzewicz, Z. W. and Doli, P.: Will groundwater ease freshwater stress under climate
714   change?, Hydrological Sciences Journal, 54, 665-675, 2009.
715   Lasslop, G., Reichstein, M., Papale, D., Richardson, A. D., Arneth, A., Barr, A., Stoy, P.,
716   and Wohlfahrt, G.: Separation of net ecosystem exchange into assimilation and
717   respiration using a light response curve approach: critical issues and global
718   evaluation, Global Change Biology, 16, 187-208, 2010.
719   Leng, G., Huang, M., Tang, Q., and Leung, L. R.: A modeling study of irrigation effects
720   on global surface water and groundwater resources under a changing climate, Journal
721   of Advances in Modeling Earth Systems, 7, 1285-1304, 2015.
722   Leng, G., Leung, L. R., and Huang, M.: Significant impacts of irrigation water sources
723   and methods on modeling irrigation effects in the ACMELand Model, Journal of
724   Advances in Modeling Earth Systems, 9, 1665-1683, 2017.
725   Leung, L. R., Huang, M., Qian, Y., and Liang, X.: Climate–soil–vegetation control on
726   groundwater table dynamics and its feedbacks in a climate model, Climate Dynamics,
727   36, 57-81, 2011.
728   Levine, J. B. and Salvucci, G. D.: Equilibrium analysis of groundwater–vadose zone
729   interactions and the resulting spatial distribution of hydrologic fluxes across a
730   Canadian Prairie, Water Resources Research, 35, 1369-1383, 1999.

731   Liang, X., Xie, Z., and Huang, M.: A new parameterization for surface and groundwater
732   interactions and its impact on water budgets with the variable infiltration capacity
733   (VIC) land surface model, Journal of Geophysical Research: Atmospheres, 108, n/a-
734   n/a, 2003.
735   Lohse, K. A., Brooks, P. D., McIntosh, J. C., Meixner, T., and Huxman3, T. E.: Interactions
736   Between Biogeochemistry and Hydrologic Systems, Annual Review of Environment
737   and Resources, 34, 65-96, 2009.
738   Marvel, K., Biasutti, M., Bonfils, C., Taylor, K. E., Kushnir, Y., and Cook, B. I.: Observed
739   and Projected Changes to the Precipitation Annual Cycle, Journal of Climate, 30, 4983-
740   4995, 2017.
741   Maxwell, R. M. and Miller, N. L.: Development of a Coupled Land Surface and
742   Groundwater Model, Journal of Hydrometeorology, 6, 233-247, 2005.
743   Miguez-Macho, G., Fan, Y., Weaver, C. P., Walko, R., and Robock, A.: Incorporating
744   water table dynamics in climate modeling: 2. Formulation, validation, and soil
745   moisture simulation, Journal of Geophysical Research: Atmospheres, 112, n/a-n/a,
746   2007.
747   Milly, P. C. D., Malyshev, S. L., Shevliakova, E., Dunne, K. A., Findell, K. L., Gleeson, T.,
748   Liang, Z., Phillipps, P., Stouffer, R. J., and Swenson, S.: An Enhanced Model of Land
749   Water and Energy for Global Hydrologic and Earth-System Studies, Journal of
750   Hydrometeorology, 15, 1739-1761, 2014.
751   Mualem, Y.: A new model for predicting the hydraulic conductivity of unsaturated
752   porous media, Water Resources Research, 12, 513-522, 1976.
753   Niu, G.-Y., Yang, Z.-L., Dickinson, R. E., and Gulden, L. E.: A simple TOPMODEL-based
754   runoff parameterization (SIMTOP) for use in global climate models, Journal of
755   Geophysical Research: Atmospheres, 110, n/a-n/a, 2005.
756   Niu, G.-Y., Yang, Z.-L., Dickinson, R. E., Gulden, L. E., and Su, H.: Development of a simple
757   groundwater model for use in climate models and evaluation with Gravity Recovery
758   and Climate Experiment data, Journal of Geophysical Research: Atmospheres, 112,
759   n/a-n/a, 2007.
760   Niu, J., Shen, C., Chambers, J. Q., Melack, J. M., and Riley, W. J.: Interannual Variation in
761   Hydrologic Budgets in an Amazonian Watershed with a Coupled Subsurface–Land
762   Surface Process Model, Journal of Hydrometeorology, 18, 2597-2617, 2017.
763   Oleson, K. W., D.M. Lawrence, G.B. Bonan, B. Drewniak, M. Huang, C.D. Koven, S. Levis,
764   F. Li, W.J. Riley, Z.M. Subin, S.C. Swenson, P.E. Thornton, A. Bozbiyik, R. Fisher, E.
765   Kluzek, J.-F. Lamarque, P.J. Lawrence, L.R. Leung, W. Lipscomb, S. Muszala, D.M.
766   Ricciuto, W. Sacks, Y. Sun, J. Tang, Z.-L. Yang: Technical Description of version 4.5 of
767   the Community Land Model (CLM), National Center for Atmospheric Research,
768   Boulder, CO, 422 pp., 2013.
769   Pacific, V. J., McGlynn, B. L., Riveros-Iregui, D. A., Welsch, D. L., and Epstein, H. E.:
770   Landscape structure, groundwater dynamics, and soil water content influence soil
771   respiration across riparian–hillslope transitions in the Tenderfoot Creek
772   Experimental Forest, Montana, Hydrological Processes, 25, 811-827, 2011.
773   Pelletier, J. D., Broxton, P. D., Hazenberg, P., Zeng, X., Troch, P. A., Niu, G.-Y., Williams,
774   Z., Brunke, M. A., and Gochis, D.: A gridded global data set of soil, intact regolith, and
775   sedimentary deposit thicknesses for regional and global land surface modeling,
776   Journal of Advances in Modeling Earth Systems, 8, 41-65, 2016.

777   Petra, D.: Vulnerability to the impact of climate change on renewable groundwater
778   resources: a global-scale assessment, Environmental Research Letters, 4, 035006,
779   2009.
780   Piao, S. L., Ito, A., Li, S. G., Huang, Y., Ciais, P., Wang, X. H., Peng, S. S., Nan, H. J., Zhao, C.,
781   Ahlström, A., Andres, R. J., Chevallier, F., Fang, J. Y., Hartmann, J., Huntingford, C., Jeong,
782   S., Levis, S., Levy, P. E., Li, J. S., Lomas, M. R., Mao, J. F., Mayorga, E., Mohammat, A.,
783   Muraoka, H., Peng, C. H., Peylin, P., Poulter, B., Shen, Z. H., Shi, X., Sitch, S., Tao, S., Tian,
784   H. Q., Wu, X. P., Xu, M., Yu, G. R., Viovy, N., Zaehle, S., Zeng, N., and Zhu, B.: The carbon
785   budget of terrestrial ecosystems in East Asia over the last two decades,
786   Biogeosciences, 9, 3571-3586, 2012.
787   Pruess, K., Oldenburg, C., and Moridis, G.: TOUGH2 User's Guide, Version 2.0,
788   Lawrence Berkeley National Laboratory, Berkeley, CALBNL-43134, 1999.
789   Rihani, J. F., Maxwell, R. M., and Chow, F. K.: Coupling groundwater and land surface
790   processes: Idealized simulations to identify effects of terrain and subsurface
791   heterogeneity on land surface energy fluxes, Water Resources Research, 46, n/a-n/a,
792   2010.
793   Salvucci, G. D. and Entekhabi, D.: Hillslope and Climatic Controls on Hydrologic Fluxes,
794   Water Resources Research, 31, 1725-1739, 1995.
795   Shen, C., Niu, J., and Phanikumar, M. S.: Evaluating controls on coupled hydrologic and
796   vegetation dynamics in a humid continental climate watershed using a subsurface-
797   land surface processes model, Water Resources Research, 49, 2552-2572, 2013.
798   Siebert, S., Burke, J., Faures, J. M., Frenken, K., Hoogeveen, J., Döll, P., and Portmann, F.
799   T.: Groundwater use for irrigation – a global inventory, Hydrol. Earth Syst. Sci., 14,
800   1863-1880, 2010.
801   Sivapalan, M., Beven, K., and Wood, E. F.: On hydrologic similarity: 2. A scaled model
802   of storm runoff production, Water Resources Research, 23, 2266-2278, 1987.
803   Soylu, M. E., Istanbulluoglu, E., Lenters, J. D., and Wang, T.: Quantifying the impact of
804   groundwater depth on evapotranspiration in a semi-arid grassland region, Hydrol.
805   Earth Syst. Sci., 15, 787-806, 2011.
806   Srivastava, R. and Yeh, T. C. J.: Analytical solutions for one-dimensional, transient
807   infiltration toward the water table in homogeneous and layered soils, Water
808   Resources Research, 27, 753-762, 1991.
809   Swenson, S. C. and Lawrence, D. M.: Assessing a dry surface layer-based soil resistance
810   parameterization for the Community Land Model using GRACE and FLUXNET-MTE
811   data, Journal of Geophysical Research: Atmospheres, 119, 10,299-210,312, 2014.
812   Swenson, S. C., Lawrence, D. M., and Lee, H.: Improved simulation of the terrestrial
813   hydrological cycle in permafrost regions by the Community Land Model, Journal of
814   Advances in Modeling Earth Systems, 4, n/a-n/a, 2012.
815   Tanaka, M., Girard, G., Davis, R., Peuto, A., and Bignell, N.: Recommended table for the
816   density of water between 0 °C and 40 °C based on recent experimental reports,
817   Metrologia, 38, 301, 2001.
818   Taylor, K. E., Stouffer, R. J., and Meehl, G. A.: An Overview of CMIP5 and the Experiment
819   Design, Bulletin of the American Meteorological Society, 93, 485-498, 2012.
820   Taylor, R. G., Scanlon, B., Döll, P., Rodell, M., Van Beek, R., Wada, Y., Longuevergne, L.,
821   Leblanc, M., Famiglietti, J. S., and Edmunds, M.: Ground water and climate change,
822   Nature Climate Change, 3, 322-329, 2013.

823   Tian, W., Li, X., Cheng, G. D., Wang, X. S., and Hu, B. X.: Coupling a groundwater model
824   with a land surface model to improve water and energy cycle simulation, Hydrol.
825   Earth Syst. Sci., 16, 4707-4723, 2012.
826   van Genuchten, M. T.: A Closed-form Equation for Predicting the Hydraulic
827   Conductivity of Unsaturated Soils1, Soil Science Society of America Journal, 44, 892-
828   898, 1980.
829   Walko, R. L., Band, L. E., Baron, J., Kittel, T. G. F., Lammers, R., Lee, T. J., Ojima, D., Sr., R.
830   A. P., Taylor, C., Tague, C., Tremback, C. J., and Vidale, P. L.: Coupled Atmosphere–
831   Biophysics–Hydrology Models for Environmental Modeling, Journal of Applied
832   Meteorology, 39, 931-944, 2000.
833   White, M. and STOMP, O. M.: Subsurface transport over multiple phases; Version 2.0;
834   Theory Guide, Pacific Northwest National Laboratory, 2000. 2000.
835   Yeh, P. J.-F. and Eltahir, E. A. B.: Representation of Water Table Dynamics in a Land
836   Surface Scheme. Part I: Model Development, Journal of Climate, 18, 1861-1880, 2005.
837   York, J. P., Person, M., Gutowski, W. J., and Winter, T. C.: Putting aquifers into
838   atmospheric simulation models: an example from the Mill Creek Watershed,
839   northeastern Kansas, Advances in Water Resources, 25, 221-238, 2002.
840   Yuan, X., Xie, Z., Zheng, J., Tian, X., and Yang, Z.: Effects of water table dynamics on
841   regional climate: A case study over east Asian monsoon area, Journal of Geophysical
842   Research: Atmospheres, 113, n/a-n/a, 2008.
843   Zektser, I. S. and Evertt, L. G.: Groundwater resources of the world and their use,
844   United Nations Educational, Scientific and Cultural Organization7, place de Fontenoy,
845   75352 Paris 07 SP, 2004.
846   Zeng, X. and Decker, M.: Improving the Numerical Solution of Soil Moisture–Based
847   Richards Equation for Land Models with a Deep or Shallow Water Table, Journal of
848   Hydrometeorology, 10, 308-319, 2009.
849   Zhu, Q., Riley, W. J., Tang, J., and Koven, C. D.: Multiple soil nutrient competition
850   between plants, microbes, and mineral surfaces: model development,
851   parameterization, and example applications in several tropical forests,
852   Biogeosciences, 13, 341-363, 2016.
853
854